Title
Comparison of the energy spectra and number fluxes from a simple flare model to observations

Journal
Solar Physics, 236(1)

ISSN
0038-0938

Authors
Hannah, Iain G
Fletcher, L

Publication Date
2006-06-01

Peer reviewed

COMPARISON OF THE ENERGY SPECTRA AND NUMBER FLUXES FROM A SIMPLE FLARE MODEL TO OBSERVATIONS.

IAIN G. HANNAH (e-mail: hannah@ssl.berkeley.edu)
Space Sciences Laboratory, University of California at Berkeley, Berkeley, CA, 94720-7450, USA

LYNDSAY FLETCHER (e-mail: lyndsay@astro.gla.ac.uk)
Department of Physics and Astronomy, University of Glasgow, Glasgow G12 8QQ, UK

Abstract. In this paper we investigate the energy spectra produced by a simple test particle X-point model of a solar flare for different configurations of the initial electromagnetic field. We find that once the reconnection electric field is larger than $1\ \mathrm{Vm}^{-1}$ the particle distribution transits from a heated one to a partially accelerated one. As we close the separatrices of the X-point and the angle in the inflow direction widens we find that more particles are accelerated out of the thermal distribution and this power-law component extends to lower energies. When we introduce a guiding magnetic field component we find that more particles are energised, but only up to a maximum energy dictated primarily by the reconnection electric field. Despite being able to accelerate particles to observable energies and demonstrate behaviour in the energy spectra that is consistent with observations, this single X-line model can only deliver the number fluxes required for microflares.

1. Introduction

Solar flares are one of the most exuberant phenomena in the solar corona. As confirmed by RHESSI spectra (Lin *et al.*, 2002) these fast, transient energy releases heat the coronal plasma to tens of MK and efficiently accelerate particles: electrons to 10s of keV and protons to 100s of MeV in around a second (Miller *et al.*, 1997). Flares are thought to be due to liberation, by magnetic reconnection, of the energy stored in the coronal magnetic field. Evidence for reconnection includes *Yohkoh* observations of cusp-shaped soft X-ray loops, with an increase of flare loop height and footpoint separation as the flare progresses (Tsuneta *et al.*, 1992; Tsuneta, 1996) and coronal hard X-ray sources (Masuda *et al.*, 1994; Tomczak, 2001). RHESSI observations show hard X-ray footpoints which separate or move along flare ribbons (Fletcher and Hudson, 2002; Krucker *et al.*, 2005), and both stationary and moving coronal sources with the expected characteristics of current sheets (Sui and Holman, 2003; Sui *et al.*, 2004). The moving footpoints and rising

cusp occur as field lines further out are brought in and reconnected, indicating an evolution of the magnetic field throughout the flare.

The reconnection electric field can produce highly energised particles, providing an attractive way to link the flare magnetic evolution directly with the accelerated particles. In this paper we will investigate a simple model for a flare acceleration region, based around a coronal X-type neutral point (X-point). Our focus is the dependence on the electromagnetic field configuration of the spectra of the energised particles. We use the *test particle* approach, in which a distribution of protons or electrons individually explore the fixed electromagnetic field geometry of the reconnection region. As this approach does not permit feedback on the field, the resulting energy spectra are only valid if the self-field of the accelerated particles has a negligible effect on the initial field. However, this method is flexible, and numerically simpler than other approaches such as Vlasov or PIC simulations. So the fundamental aspects of the energisation process are readily apparent.

A substantial literature already exists on the problem of test-particle acceleration in a reconnecting magnetic field, normally studying the current sheet or X-point in 2D. An applied electric field perpendicular to the reconnecting field drifts the particles through the reconnection region and energises them. Close to the X-point the particles are non-adiabatic, since their gyroradius is larger than the magnetic field scale length, and can be directly accelerated by the electric field. The size of this region has been found to depend on the applied electric field, and the angle between the X-point separatrices (Astrom, 1956; Speiser, 1965; Friedman, 1969; Rushbridge, 1971; Sonnerup, 1971; Bulanov and Sasorov, 1976). The time spent by particles in this region scales with the applied electric field E_0, as $\tau \approx E_0^{-1/3}$ and the final energy varies as $E_0^{4/3}$ (Burkhart *et al.*, 1990; Vekstein and Priest, 1995). It has been found analytically and numerically that a Maxwellian distribution of particles passing through the reconnection region results in energy spectra that are exponential at high energies (Bulanov and Sasorov, 1976; Deeg *et al.*, 1991; Bruhwiler and Zweibel, 1992; Moses *et al.*, 1993). Considering only the behaviour of the particles outwith the non-adiabatic region, a power-law spectrum was found with energised particles moving away from the X-point, close to the separatrices, as jets (Vekstein and Browning, 1997).

The X-point system has also been studied when there is a non-zero guide magnetic field (parallel to the applied electric field). A guide field helps to accelerate particles, as they can directly gyrate along it in the direction of the electric field (Litvinenko, 1996). The energy spectra for these 2.5D models have again been found generally to be exponentially

decreasing (Bulanov, 1980; Bruhwiler and Zweibel, 1992; Nocera *et al.*, 1996). However some studies suggest that a power-law spectrum would be produced (Mori *et al.*, 1998; Browning and Vekstein, 2001). Analysis has consistently shown that with a guiding magnetic field the accelerated particles escape the reconnection region along the separatrices; which separatrix depends on the particle charge (Bulanov, 1980; Zhu and Parks, 1993; Zharkova and Gordovskyy, 2004; Wood and Neukirch, 2005; Hamilton *et al.*, 2005). The separation of electron and ion populations is more pronounced for higher guide fields. In more advanced field configurations, test particles explore electromagnetic fields derived from MHD reconnection models in 2D (Sakai, 1992; Petkaki and MacKinnon, 1997; Hamilton *et al.*, 2003) or 3D (Schopper *et al.*, 1999), as well as in analytical steady state 3D reconnecting fields (Dalla and Browning, 2005).

While the ability of reconnection electric fields to accelerate particles is well-established, several questions regarding the applicability of the mechanism to flares remain un-addressed, including overall particle fluxes available, and the dependence of the spectra on magnetic field parameters. In this paper we study the acceleration of particles close to a single X-line for different configurations of the electromagnetic field, that are expected to vary as the flare progresses. We study the opening angle of the magnetic separatrices, the guiding magnetic field and applied electric field. We also want to quantify the effect these changes have on the accelerated versus "heated" distributions and to investigate how this compares to flare observations.

In Section 2 we introduce the flare model and demonstrate some of the test particle behaviour in the system. In Section 3 we calculate the energy spectra for the particles under different field configurations and show what fraction of particles are energised. In Section 4 we compare these results to flare observations and discuss the applicability of the model and conclude in Section 5.

2. System Setup

2.1. Model Configuration

The magnetic X-point can be described by the electromagnetic field configuration given as

$$\mathbf{B} = B_0(\alpha^2 y, x, \kappa), \qquad \mathbf{E} = (0, 0, E_0) \tag{1}$$

where α has a range of $0 < \alpha \leq 1$ and $\tan^{-1}(\alpha)$ is the angle between the separatrix and the y-axis. The parameter κ is either 0 or a

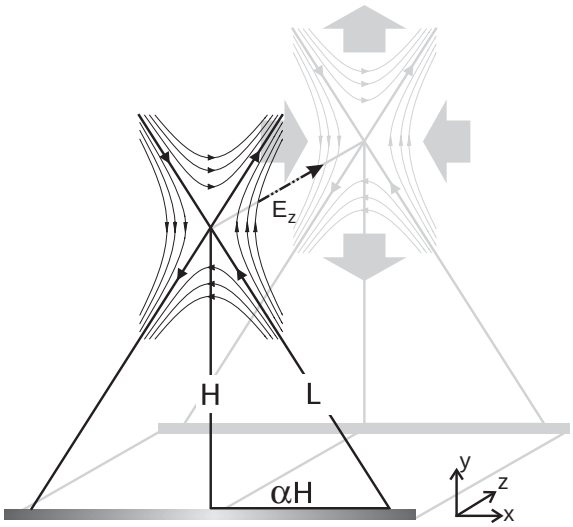

Figure 1. The X-point model of a solar flare. The extension of the 2-dimensional X-point geometry is achieved by having an invariance in the electromagnetic fields in the z-direction, indicated by the grey recessed X-point. Also shown is the direction of the $\mathbf{E} \times \mathbf{B}$ drift, indicated by the thick grey arrows, and the extension of the separatrices down to the photosphere, which provides the scaling for the magnetic field.

constant value, representing the guiding magnetic field strength in the z-direction.

Equations (1) are scaled by assuming that the origin is at a height of H above the photosphere, with a magnetic field strength of $B_{\rm fp}$ occurring at the point where the separatrices meet the photosphere as shown in Figure 1. We take $B_0 = B_{\rm fp}/(\alpha L)$ in Equation (1), where L is the distance along the separatrices between the origin and the photosphere and this is given by $L = H(1+\alpha^2)^{1/2} = H\theta$, defining θ in the process. Taking a typical flaring coronal acceleration height of $H = 10^7$ m and photospheric magnetic field strength of $B_{\rm fp} = 0.01$ T, gives $B_0 = 10^{-9}/(\alpha\theta)$ Tm^{-1}. We scale times by the gyroperiod τ_i at a distance $r = D_i$ from the origin (with subscript i denoting the species of particle) and velocities by the speed of light c. So our distances are scaled by $D_i = c\tau_i = (cm_iH/(|q|B_{\rm fp}))^{1/2}$, where m_i is the mass of the particle and q is the particle's charge. Since the constant κ is also in Equation (1), it too is scaled by D_i. The scaled electric field is taken as $\tilde{E_0} = E_0H/(cD_iB_{\rm fp})$. These fields have been scaled over a relatively large distance compared to the scale of the particle dynamics, i.e. $H >> D_i$. This is so that we can physically model particle acceleration above an arcade of loops on the Sun. However in practice we are only considering the particle behaviour close to the neutral point, $\approx D_i$, and

so the electric field is limited to this region, rather than applied over H. This also means that the particles can escape the X-point in the sense that they move outwith the region of calculation within the short time for which we follow them.

2.2. Equations of Motion & Non-Adiabatic Region

The relativistic equations of motion of a charged particle in the X-point are found by substituting Equation (1) into the Lorentz equation. We find that the scaled equations for the particle in our system are

$$\frac{\mathrm{d}x}{\mathrm{d}t} = \frac{p_\mathrm{x}}{\gamma}, \qquad \frac{\mathrm{d}y}{\mathrm{d}t} = \frac{p_\mathrm{y}}{\gamma}, \qquad \frac{\mathrm{d}z}{\mathrm{d}t} = \frac{p_\mathrm{z}}{\gamma} \tag{2}$$

$$\frac{\mathrm{d}p_\mathrm{x}}{\mathrm{d}t} = \frac{\epsilon}{\alpha\theta}\left[\kappa\frac{\mathrm{d}y}{\mathrm{d}t} - x\frac{\mathrm{d}z}{\mathrm{d}t}\right] \tag{3}$$

$$\frac{\mathrm{d}p_\mathrm{y}}{\mathrm{d}t} = \frac{\epsilon}{\alpha\theta}\left[\alpha^2 y\frac{\mathrm{d}z}{\mathrm{d}t} - \kappa\frac{\mathrm{d}x}{\mathrm{d}t}\right] \tag{4}$$

$$\frac{\mathrm{d}p_\mathrm{z}}{\mathrm{d}t} = \frac{\epsilon}{\alpha\theta}\left[x\frac{\mathrm{d}x}{\mathrm{d}t} - \alpha^2 y\frac{\mathrm{d}y}{\mathrm{d}t}\right] + \epsilon\tilde{E}_0 \tag{5}$$

where $\epsilon = q/|q|$ so $\epsilon = 1$ for protons and $\epsilon = -1$ for electrons, $\tilde{E}_0$ is the scaled electric field, γ is the Lorentz factor and, because of the scaling, $\gamma^2 = 1 + \mathbf{p}^2$. This means that the kinetic energy of the particle is $W = \gamma - 1$, scaled by the rest mass. Equations (2–5) represents the behaviour of either electrons or protons but over different temporal and spatial scales: the scaling is $(m_\mathrm{p}/m_\mathrm{e})^{1/2} \approx 43$ times bigger for the protons than electrons. Of the equations of motion only Equation (5) is solvable analytically and so we have to numerically integrate them to follow a test particle's journey through the X-point.

The size of the non-adiabatic region about the X-line can be estimated as in Rushbridge (1971) and Sonnerup (1971) which in our scaled system is

$$\Delta = \sqrt{\alpha\theta\zeta v_\perp}. \tag{6}$$

on either the x-, y-axis or separatrix, represented by $\zeta = 1$, $= \alpha^{-2}$ and $= \alpha^{-1}$ respectively. If $\alpha = 1$ (i.e. the separatrices perpendicular to each other), then Δ is constant forming a circular region about the X-line. If $\alpha < 1$, then the angle between the separatrices and the y-axis reduces, and the size of Δ is larger in the y-direction and smaller in the x-direction. The size is also dependent on $v_\perp$ and this can be estimated from either the initial thermal velocity or electric field drift, depending on which is larger. For a temperature of $T = 1$ MK, and $\alpha = 1$, we find that $\Delta_\mathrm{Tp} = 0.025 D_\mathrm{p} = 1377$ m for protons and $\Delta_\mathrm{Te} = 0.161 D_\mathrm{e} = 210$ m for electrons. Once $E_0 \gtrsim 0.1$ Vm^{-1} for protons and $E_0 \gtrsim 1.0$ Vm^{-1}

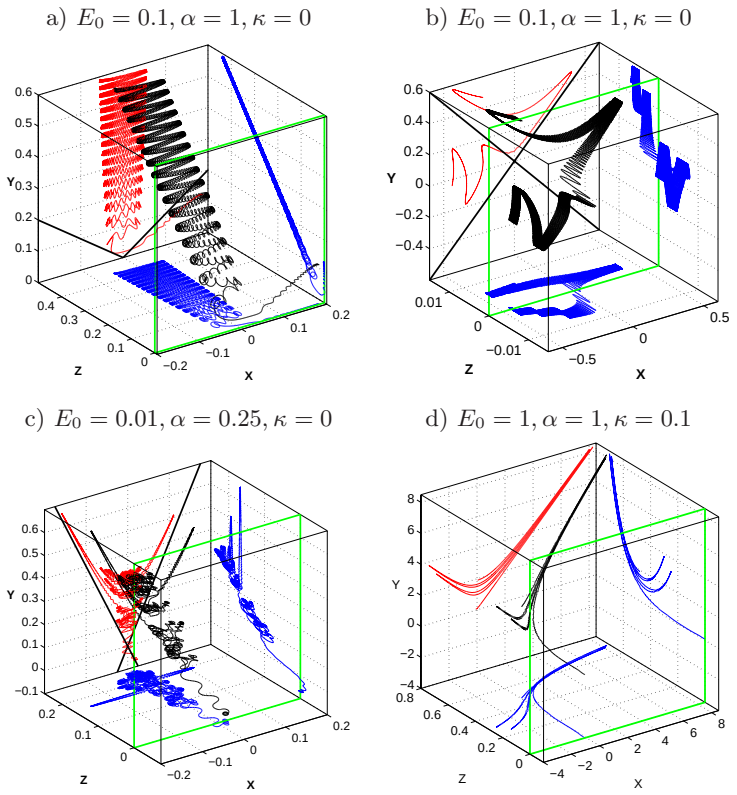

Figure 2. Four test particle orbits numerically found for different starting positions in phase space with the band around the box indicating where the particles started. The black line is the 3D orbit, the bottom, righthand and back walls show the x-z, y-z and x-y projections of the orbit, respectively. Above each orbit the magnitude of the perpendicular electric field (E_0, given in Vm^{-1}) and the angle between the separatrices (α) and parallel magnetic field component (κ) are given.

for electrons the electric field drift dominates over the initial thermal motion.

2.3. Numerical Setup & Example Orbits

To numerically integrate Equations (2–5) have used the 8^{th} order fixed step integrator of Prince and Dormand (1981), as we found it to be robust for this system. We start each test particle with a random x-y position in a box of $\pm 10\Delta_{\mathrm{T}}$ around the X-point in the z=0 plane and each component of a particle's initial momentum is drawn randomly from Maxwellian distributions that correspond to the particles having an initial thermal energy distribution of 1 MK. We follow the test particles for a fixed time corresponding to the acceleration timescales for

a) Protons after 1 second α varying.

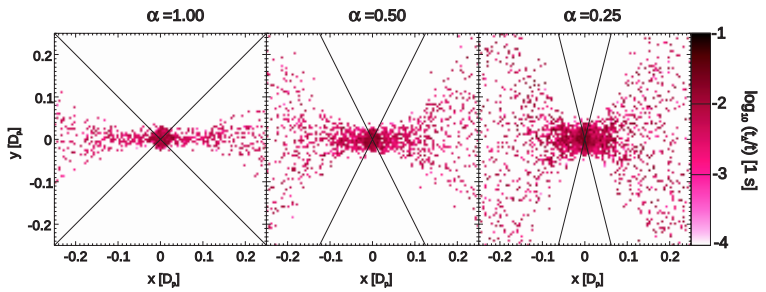

b) Protons after 1 second κ varying.

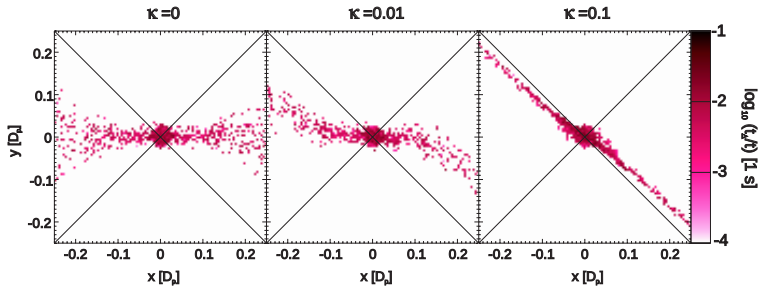

Figure 3. Density plots of the fraction of time spent in the non-adiabatic region as a function of initial x-y position, for protons after 1 second as a) α or b) κ varies for 10^4 protons with $E_0 = 1$ Vm^{-1}.

these particles in flares (Aschwanden, 2002): 0.1 seconds for electrons and 1 second for protons.

Some example proton orbits for different system configuration and initial starting positions are shown in Figure 2. Figure 2a) shows a highly accelerated orbit, and 2b) an orbit that drifts through the reconnection region. In Figure 2c) the separatrices are no longer perpendicular, as $\alpha = 0.25$ and although this orbit appears to be highly accelerated it is clear that the particle has been irregularly gyrating between the separatrices as it moves through the non-adiabatic region. So it has not travelled as far in the z-direction and gained less energy than the purely accelerated orbit of Figure 2a), when $\alpha = 1$. In Figure 2d) the separatrices are again perpendicular but now there is a guiding magnetic field component, $\kappa = 0.1$. As expected this particle is ejected out close to the separatrices.

2.4. Dependence on Initial Position

Following a Maxwellian distribution of 10^4 particles for a variety of starting conditions allows us to explore dependence on the initial phase-

space position, which helps to explain the results we see in the energy spectra in Section 3. In Figure 3 we have plotted the fraction of time that protons spend within Δ of the X-point, as a function of their initial x-y position, since it is how long the particles spend in this region that will be the dominating factor in how much energy they gain (Deeg *et al.*, 1991; Heerikhuisen *et al.*, 2002).

In Figure 3a) we have decreased the α parameter, which closes the separatrices in the y-direction. This widens the reconnection region in the inflow region resulting in considerably more protons spending time in the non-adiabatic region and gaining energy. In Figure 3b) we have increased the κ parameter, which introduces a guiding component of the magnetic field. As this field increases the initial beam in phase-space twists, which is due to the additional curvature and gradient drift introduced in the x,y plane. In these simulations all the protons are ejected along the $x = y$ separatrix and those that started below the $y = -x$ separatrix move to the bottom left and those above it move to the top right. This is the expected result as discussed in Section 1. However this figure is slightly deceptive as once $\kappa \geq \Delta$, as in the right panel in 3b), there is no unmagnetised non-adiabatic region about the X-line. This means that particles within κ of the X-line but outwith Δ can also be highly energised, although those within Δ gain the most energy.

3. Energy Spectra

3.1. Varying Electric Field Strength

In Figure 4 we show the energy spectra (lefthand column) and energy gain histograms (righthand column) for 10^4 a) protons and b) electrons, obtained for different values of the electric field after 1 second and 0.1 seconds respectively. From the energy spectra we quickly see that, as well as "heating" (i.e. an upwards shift in the overall energy distribution) we can get protons energised to levels of interest for γ-ray line production (a few MeV and above) within one second, but only for the largest $E_0 \geq 10$ Vm^{-1}. Following the particles for longer integration times would not produce substantial further acceleration since the protons started close to the neutral point and so have already had the opportunity to gain the most energy. We also get electrons accelerated to observable energies (10s of keV) within 0.1 seconds, once $E_0 \geq 1$ Vm^{-1}.

Table I. The percentage of 10^4 electrons and then protons that have final kinetic energies greater than some level (given in eV) after 0.1 and 1 seconds respectively, as we change the initial applied electric field E_0.

E_0 (Vm^{-1})	% of electrons after 0.1 sec with W				% of protons after 1 sec with W			
	$> 10^3$	$> 10^4$	$> 10^5$	$> 10^6$	$> 10^3$	$> 10^4$	$> 10^5$	$> 10^6$
0.001	0.0	0.0	0.0	0.0	0.0	0.0	0.0	0.0
0.01	0.03	0.0	0.0	0.0	0.0	0.0	0.0	0.0
0.1	5.45	0.0	0.0	0.0	4.35	0.0	0.0	0.0
1.0	29.40	3.61	0.0	0.0	48.16	11.24	0.40	0.0
10.0	95.73	47.48	11.97	0.02	100.0	100.0	58.53	11.40

a) Protons with $\alpha = 1, \kappa = 0$ after 1 second.

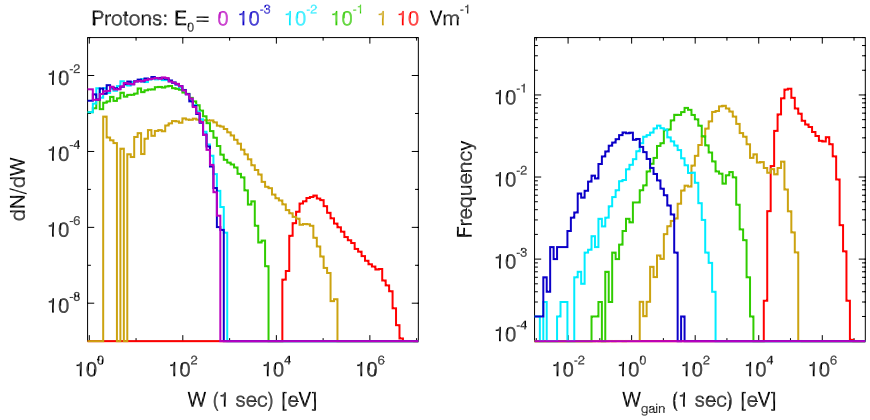

b) Electrons with $\alpha = 1, \kappa = 0$ after 0.1 seconds.

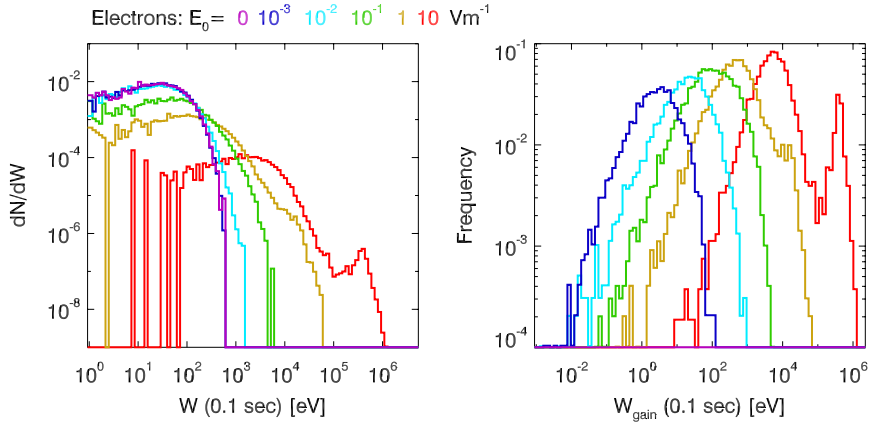

Figure 4. The energy spectra (lefthand column) and the kinetic energy gain (right-hand column) for the distribution of a) protons and b) electrons with different magnitudes of the applied electric field E_0.

Table II. The percentage of 10^4 electrons and protons that have final kinetic energies greater than some level (given in eV) after 0.1 and 1 seconds respectively, as we change the angle between the separatrices α.

α	% of electrons after 0.1 sec with W				% of protons after 1 sec with W			
	$> 10^{2.5}$	$> 10^{3}$	$> 10^{3.5}$	$> 10^{4}$	$> 10^{3}$	$> 10^{3.5}$	$> 10^{4}$	$> 10^{4.5}$
1.00	65.29	29.64	9.81	4.10	47.99	21.97	11.14	5.47
0.75	61.94	27.20	11.35	3.44	47.59	24.20	14.30	5.81
0.50	53.30	27.48	9.97	1.00	57.49	34.79	20.99	3.15
0.25	47.32	19.11	4.19	0.31	72.61	48.15	18.79	2.94

a) Protons with $E_0 = 1$ Vm^{-1} and $\kappa = 0$ after 1 second.

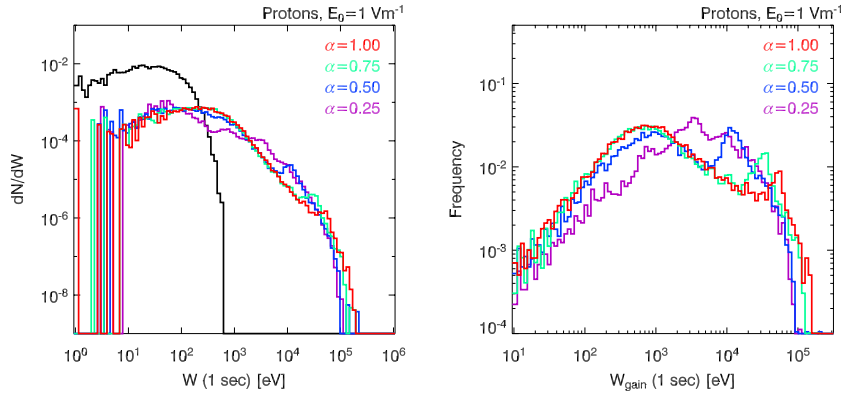

b) Electrons with $E_0 = 1$ Vm^{-1} and $\kappa = 0$ after 0.1 seconds.

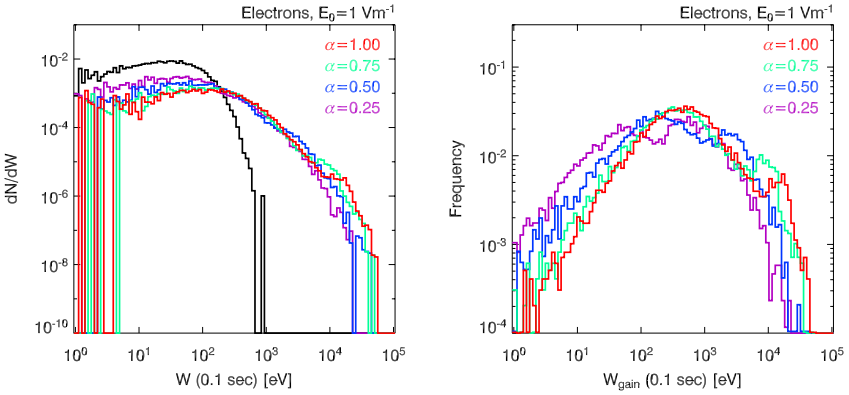

Figure 5. The energy spectra (lefthand column) and the kinetic energy gain (right-hand column) for the distribution of a) protons and b) electrons with different angles between the separatrices α.

Table III. The percentage of 10^4 electrons and then protons that have final kinetic energies greater than some level (given in eV) after 0.1 and 1 seconds respectively, as we change the applied magnetic field z-component, κ.

κ	% of electrons after 0.1 sec with W				% of protons after 1 sec with W			
	$> 10^{2.5}$	$> 10^3$	$> 10^{3.5}$	$> 10^4$	$> 10^3$	$> 10^{3.5}$	$> 10^4$	$> 10^{4.5}$
0.00	64.95	29.47	9.75	4.08	48.19	21.87	11.06	5.43
0.01	66.79	29.07	9.66	3.72	97.51	30.77	10.52	4.78
0.10	96.80	37.55	9.95	3.09	100.00	100.00	99.56	38.08

a) Protons with $E_0 = 1$ Vm^{-1} and $\alpha = 1$ after 1 second.

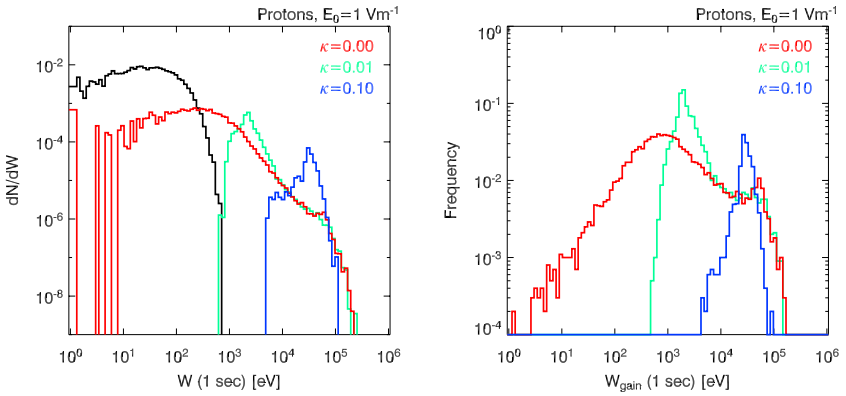

b) Electrons with $E_0 = 1$ Vm^{-1} and $\alpha = 1$ after 0.1 seconds.

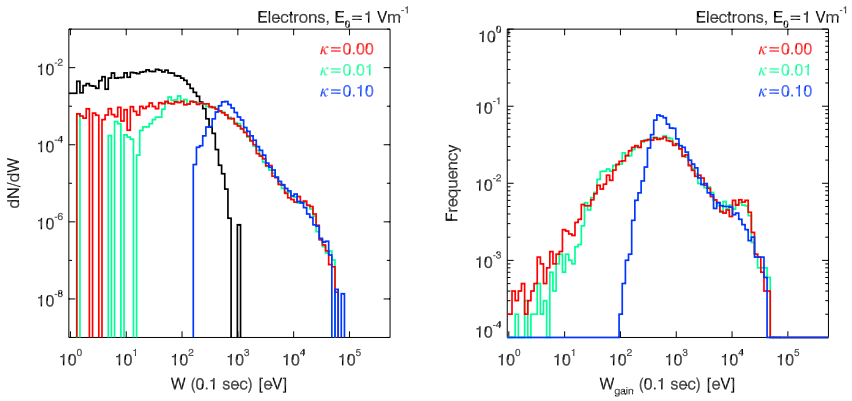

Figure 6. The energy spectra (lefthand column) and the kinetic energy gain (right-hand column) for the distribution of a) protons and b) electrons with different magnitudes of the parallel component of the magnetic field κ.

This is further highlighted in Table I where we have calculated, for each value of E_0, the percentage of test particles that surpass different energy thresholds. Again we see that protons are accelerated to energies in the range of interest for γ–rays for $E_0 \geq 10\ \mathrm{Vm}^{-1}$. With the electrons we see that 29.4% have keV energies, 3.6% have 10s of keV energies with $E_0 = 1\ \mathrm{Vm}^{-1}$. More than 95.7% have keV energies and 47.5% 10s of keV energies when $E_0 = 10\ \mathrm{Vm}^{-1}$.

The shape of the energy spectra, shown in Figure 4, has properties in common with the exponentially decreasing spectrum (Bulanov and Sasorov, 1976; Deeg *et al.*, 1991; Bruhwiler and Zweibel, 1992; Moses *et al.*, 1993), but differs in two ways. Firstly at low energies the spectrum turns over or cuts off completely and does not flatten as the theoretical ones do. This is because the analytical treatment assumes a steady inflow of test particles instead of the single distribution we start at $t = 0$ and pass once through the system. The other difference is that at higher energies once a large electric field is applied ($E_0 \geq 0.1\ \mathrm{Vm}^{-1}$ for the protons and $E_0 \geq 1\ \mathrm{Vm}^{-1}$ for the electrons) a bump in the energy spectra appears. This is an additional component of particles highly accelerated out of the thermal distribution and is more evident in the energy gain histograms in Figure 4. At energies above this bump the energy spectra are more power-law in shape and decrease at a different rate than at lower energies. The bump appears once the electric field dominates the particle dynamics: i.e. when the electric field drift is larger than the initial thermal velocity. We find that in this range of the electric field we approximately gain the predicted scaling relations (see Section 1) for the time within the non-adiabatic region and energy gain (Burkhart *et al.*, 1990; Vekstein and Priest, 1995).

3.2. Varying the Angle Between the Separatrices

The effect of changing the angle between the separatrices, reducing α but keeping $E_0 = 1\ \mathrm{Vm}^{-1}$ and $\kappa = 0$, is shown in the energy spectra and energy gain histograms for 10^4 a) protons and b) electrons in Figure 5. In Table II we have calculated the percentage of test particles energised above different threshold energies for each α. Three things are immediately clear: as α decreases the "heated" component of the distribution moves to a slightly higher energy, more particles are accelerated out of the thermal distribution into the bump in the tail, and this bump occurs at lower energies. The length of the non-magnetised region in the inflow direction increases as α decreases, so this makes it easier for more particles to get into the non-adiabatic region and be energised. However the particles that gain the most energy occur when $\alpha = 1$, as when $\alpha \neq 1$ there is more opportunity for them to irregularly gyrate

about the separatrices as they pass through the reconnection region, see Figure 2c). The difference in the proton and electron behaviour for the same α is due to the same unscaled electric field being applied: for the electrons the *scaled* electric field is larger and dominates the dynamics, lessening the effect of the α decrease.

3.3. Varying the Guiding Magnetic Field

The effect of adding a guiding z-component of the magnetic field, increasing κ, but keeping $E_0 = 1$ Vm^{-1} and $\alpha = 1$, is shown in the energy spectra and energy gain histograms for 10^4 a) protons and b) electrons in Figure 6. In Table III we have calculated the percentage of test particles energised above different energy thresholds for each κ. With the guiding field there is a clear low energy cut-off to the distribution, which moves to higher energies as κ increases, so all the particles are gaining a substantial amount of energy. However, the maximum particle energies are the same as when $\kappa = 0$ since there is a finite distance a particle can travel in the integration time; κ merely aids them on their journey. Also the distribution at high energies is a power-law which slightly hardens for the electrons as κ is increased. The large difference between the proton and electron distributions is due to the magnitude of κ, given in D_i, compared to the size of the non-adiabatic region: $\kappa = 0.1$ is $> \Delta_{\rm p}$ but is $\sim \Delta_{\rm e}$ and so will dominate the proton dynamics more than the electron. The other effect, that is not apparent in these energy spectra, is that the electrons and protons are ejected from the reconnection region by different separatrices as κ increases, see Section 1, particularly at high energies. So we would expect to see different spectra and particle species at different footpoints.

4. Comparison to Flare Observations

During the impulsive phase of flares, footpoints that separate parallel to the photospheric neutral line may correspond to an increasing shear in the reconnecting field (Bogachev *et al.*, 2005). This in our model is an increasing κ and we found that this produces more heated and accelerated particles. Approaching footpoints imply the reconnection of successively less-sheared field (Somov *et al.*, 2002; Ji *et al.*, 2006), which would be a reduction in κ and with fewer heated and accelerated particles. This might go some way to explaining the finding of (Sakao *et al.*, 1998) that separating HXR footpoint sources are associated with a superhot plasma component and spectra breaking upwards, i.e. harder spectra, whereas flares having footpoints that approach or remain at a constant separation have no superhot sources and softer spectra.

As the flare evolves the reconnection region is expected to rise as evidenced by the growing *Yohkoh* soft X-ray "cusp" (Forbes and Acton, 1996) or RHESSI observations of rising coronal sources (Sui *et al.*, 2004), corresponding to a decrease in α. The reconnection electric field and the shear (or guiding) component (κ) should also decrease, with the reconnection of weaker and less sheared field anchored more distant from the neutral line. Our simulations predict that this would lead to a slight steepening of the spectrum and a reduction of the number of non-thermal particles, so there would be a larger "heated" versus accelerated component of the energy spectra. In the majority of flares, both a spectral softening and an increased heating are observed in the later phases.

Interpretations of flare footpoint motion based on a 2D reconnection scenario imply impulsive phase electric fields of several hundred Vm^{-1} (Qiu *et al.*, 2002; Asai *et al.*, 2004). Therefore there is no issue with obtaining electron *energies* observed in flares. However, the requirement to deliver the number flux inferred from observations (of up to 10^{36} electrons s^{-1} for over 10s seconds for the largest flares (Holman *et al.*, 2003), using the usual assumptions of collisional thick–target bremsstrahlung) is always more problematic. To estimate how bad the number problem is for this *single* X-line model we can calculate the continuous electron acceleration by considering the resupply of electrons via the inward flow. Approximately, the flux is $F_{\mathrm{acc}} = f n_{\mathrm{e}} v_{\mathrm{E}} A$ where A is the area of the acceleration volume presented to the inflow of speed v_{E}, a fraction f of which is accelerated. For A, we use half of the simulation box, $200\Delta_{\mathrm{T}}^2$, multiplied by the typical X-line z-extent, on the order of 10" (7.3×10^6 m). The fraction of electrons accelerated decreases rapidly towards the edge of the box in Figure 3, so a larger A would provide a reduced f, as well as a smaller inflow speed since $v_{\mathrm{E}} \approx E_0/r$. So at the simulation box boundary, with $E_0 \sim 1\ \mathrm{Vm}^{-1}$ and taking a typical density of $10^{15}\mathrm{m}^{-3}$ gives us $F_{\mathrm{acc}} \approx 10^{31}\ f$. From Table I, $E_0 \gtrsim 1\ \mathrm{Vm}^{-1}$ accelerates about 4% of the electron distribution to < 10 keV in 0.1s, giving us a number flux of $F_{\mathrm{acc}} \approx 4{\times}10^{29}$ electrons s^{-1} - about six orders of magnitude below requirements of larger flares. This model however, might be able to account for the fluxes seen in microflares if the acceleration occurred in a dense corona, as the X-ray footpoints of microflares have been observed with $\sim$ 10" separations (Krucker *et al.*, 2002).

In our simulations, elongating the X-line towards a current sheet (decreasing α), or increasing the guide-field component, does not result in a higher number of accelerated electrons. Thus it appears that a *single* X-line configuration cannot on its own provide sufficient accelerated electrons to explain the fluxes implied by the collisional thick–target

bremsstrahlung model. Other authors, e.g. (Litvinenko, 2000) have calculated that the additional "vertical" extent provided by a current sheet of order 10^9 cm high can address the number problem. It remains to be seen whether such a narrow, vertically-elongated structure would remain stable, or would fragment into a number of X-lines as expected from the tearing-mode instability (Kliem, 1994). If the current sheet does fragment, then to obtain the required electron flux in this manner demands fragmentation into around $10^6 - 10^7$ separate X-lines. However the very precise relationship between electron spectral index and flux points to a coherent rather than entirely stochastic acceleration process (Grigis and Benz, 2004), so if an ensemble of X-lines does exist, acceleration in each should still be determined by some larger scale magnetic and electric field.

5. Conclusions

We have presented numerical simulations of the acceleration of test electrons and protons at a reconnecting X-line with an imposed guiding component of the magnetic field. They support the theoretical conclusion that the bulk of acceleration will occur within a few times the particle gyroradius from the X-line. This volume constraint means that a model with a single X-line fails to provide the electron flux inferred from flare hard X-ray observations, for anything other than a microflare. Other aspects of the spectral evolution with expected magnetic field evolution agree with some observational characteristics, suggesting it maybe applicable for smaller flares. As the "beam" component typically found in these simulations only contains a small fraction of all the particles, we are justified in the test particle approach. To explain larger flares we need to let the test particles explore other field configurations, possibly more realistic than the 2D X-line. It should also be emphasised that the large number flux required rests on the assumptions of the collisional thick–target model, in which the conversion of electron energy to HXR photon energy is at an efficiency of $\sim 10^{-5}$. Finding a way around this might alleviate the number problem in general, and for this model in particular.

Acknowledgements

The majority of this work was conducted whilst I. Hannah was a PPARC funded postgraduate student. The authors would like to thank the anonymous referee for his/her helpful comments and criticisms, which led to significant improvements in the paper.

References

Asai, A., T. Yokoyama, M. Shimojo, S. Masuda, H. Kurokawa, and K. Shibata: 2004, *Astrophys. J.* **611**, 557.

Aschwanden, M. J.: 2002, *Particle Acceleration and Kinematics in Solar Flares*. Kluwer Academic Publishers.

Astrom, E.: 1956, *Tellus* **8**, 260

Bogachev, S. A., B. V. Somov, T. Kosugi, and T. Sakao: 2005, *Astrophys. J.* **630**, 561.

Browning, P. K. and G. E. Vekstein: 2001, *J. Geophys. Res.* **106**, 18677.

Bruhwiler, D. L. and E. G. Zweibel: 1992, *J. Geophys. Res.* **97**, 10825.

Bulanov, S. V.: 1980, *Soviet Astronomy Letters* **6**, 206.

Bulanov, S. V. and P. V. Sasorov: 1976, *Soviet Astronomy* **19**, 464.

Burkhart, G. R., J. F. Drake, and J. Chen: 1990, *J. Geophys. Res.* **95**, 18833.

Dalla, S. and P. K. Browning: 2005, *Astron. Astrophys.* **436**, 1103.

Deeg, H., J. E. Borovsky, and N. Duric: 1991, *Physics of Fluids B*, **3**, 2660.

Fletcher, L. and H. S. Hudson: 2002, *Solar Phys.* **210**, 307.

Forbes, T. G. and L. W. Acton: 1996, *Astrophys. J.* **459**, 330.

Friedman, M.: 1969, *Phys. Rev.* **182**, 1408.

Grigis, P. C. and A. O. Benz: 2004, *Astron. Astrophys.* **426**, 1093.

Hamilton, B., L. Fletcher, K. G. McClements, and A. Thyagaraja: 2005, *Astrophys. J.* **625**, 496.

Hamilton, B., K. G. McClements, L. Fletcher, and A. Thyagaraja: 2003, *Solar Phys.* **214**, 339.

Heerikhuisen, J., Y. E. Litvinenko, and I. J. D. Craig: 2002, *Astrophys. J.* **566**, 512.

Holman, G. D., L. Sui, R. A. Schwartz, and A. G. Emslie: 2003, *Astrophys. J.* **595L**, L97.

Ji, H., G. Huang, H. Wang, T. Zhou, Y. Li, Y. Zhang, and M. Song: 2006, *Astrophys. J.* **636L**, L173.

Kliem, B.: 1994, *Astrophys. J.* **90**, 719.

Krucker, S., S. Christe, R. P. Lin, G. J. Hurford, and R. A. Schwartz: 2002, *Solar Phys.* **210**, 445.

Krucker, S., M. D. Fivian, and R. P. Lin: 2005, *Adv. Space Res.* **35**, 1707.

Lin, R. P. et al.: 2002, *Solar Phys.* **210**, 3.

Litvinenko, Y. E.: 1996, *Astrophys. J.* **462**, 997.

Litvinenko, Y. E.: 2000, *Solar Phys.* **194**, 327.

Masuda, S., T. Kosugi, H. Hara, S. Tsuneta, and Y. Ogawara: 1994, *Nature* **371**, 495.

Miller, J. A., P. J. Cargill, A. G. Emslie, G. D. Holman, B. R. Dennis, T. N. Larosa, R. M. Winglee, S. G. Benka, and S. Tsuneta: 1997, *J. Geophys. Res.* **102**, 14631.

Mori, K., J. Sakai, and J. Zhao: 1998, *Astrophys. J.* **494**, 430.

Moses, R. W., J. M. Finn, and K. M. Ling: 1993,*J. Geophys. Res.* **98**, 4013.

Nocera, L., F. Pegoraro, S. V. Bulanov, and G. Bertin: 1996, *Physica Scripta Volume T* **63**, 197.

Petkaki, P. and A. L. MacKinnon: 1997, *Solar Phys.* **172**, 279.

Prince, P. J. and J. R. Dormand: 1981, *J. Comp. Appl. Math* **7**, 67.

Qiu, J., J. Lee, D. E. Gary, and H. Wang: 2002, *Astrophys. J.* **565**, 1335.

Rushbridge, M. G.: 1971, *Plasma Phys.* **13**, 977.

Sakai, J.: 1992, *Solar Phys.* **140**, 99.

Sakao, T., T. Kosugi, and S. Masuda: 1998, In: *ASSL Vol. 229: Observational Plasma Astrophysics : Five Years of YOHKOH and Beyond*. 273.

Schopper, R., G. T. Birk, and H. Lesch: 1999, *Phys. Plasmas* **6**, 4318.
Somov, B. V., T. Kosugi, H. S. Hudson, T. Sakao, and S. Masuda: 2002, *Astrophys. J.* **579**, 863.
Sonnerup, B. U. O.: 1971, *J. Geophys. Res.* **76**, 8211.
Speiser, T. W.: 1965, *J. Geophys. Res.* **70**, 4219.
Sui, L. and G. D. Holman: 2003, *Astrophys. J.* **596L**, L251.
Sui, L., G. D. Holman, and B. R. Dennis: 2004, *Astrophys. J.* **612**, 546.
Tomczak, M.: 2001, *Astron. Astrophys.* **366**, 294.
Tsuneta, S.: 1996, *Astrophys. J.* **464**, 840.
Tsuneta, S., H. Hara, T. Shimizu, L. W. Acton, K. T. Strong, H. S. Hudson, and Y. Ogawara: 1992, *Publ. Astron. Soc. Japan* **44**, L63.
Vekstein, G. E. and P. K. Browning: 1997, *Phys. Plasmas* **4**, 2261.
Vekstein, G. E. and E. R. Priest: 1995, *Phys. Plasmas* **2**, 3169.
Wood, P. and T. Neukirch: 2005, *Solar Phys.* **226**, 73.
Zharkova, V. V. and M. Gordovskyy: 2004, *Astrophys. J.* **604**, 884.
Zhu, Z. and G. Parks: 1993, *J. Geophys. Res.* **98**, 7603.